

1 **Variability of vertical structure of precipitation with sea surface temperature over the**
2 **Arabian Sea and the Bay of Bengal as inferred by TRMM PR measurements**

3 **Kadiri Saikranthi¹, Basivi Radhakrishna², Thota Narayana Rao² and**

4 **Sreedharan Krishnakumari Satheesh³**

5 ¹ *Department of Earth and Climate Science, Indian Institute of Science Education and*
6 *Research (IISER), Tirupati, India.*

7 ² *National Atmospheric Research Laboratory, Department of Space, Govt. of India, Gadanki*
8 *- 517112, India.*

9 ³ *Divecha Centre for Climate Change, Centre for Atmospheric and Oceanic Sciences, Indian*
10 *Institute of Science, Bangalore - 560012, India.*

11

12

13

14

15

16

17

18

19

20

21

22

23

24

25

26

27

28

29

30 **Address of the corresponding author**

31 Dr. K. Saikranthi,

32 Department of Earth and Climate Science,

33 Indian Institute of Science Education and Research (IISER),

34 Tirupati,

35 Andhra Pradesh, India.

36 Email: ksaikranthi@gmail.com

37 **Abstract**

38 Tropical Rainfall Measuring Mission precipitation radar measurements are used to
39 examine the variation of vertical structure of precipitation with sea surface temperature (SST)
40 over the Arabian Sea (AS) and Bay of Bengal (BOB). The variation of reflectivity and
41 precipitation echo top with SST is remarkable over the AS but small over the BOB. The
42 reflectivity increases with SST (from 26°C to 31°C) by ~1 dBZ and 4 dBZ above and below
43 6 km, respectively, over the AS while, its variation is < 0.5 dBZ over the BOB. The
44 transition from shallow storms at lower SSTs ($\leq 27^\circ\text{C}$) to deeper storms at higher SSTs is
45 strongly associated with the decrease in stability and mid-tropospheric wind shear over the
46 AS. Contrary, the storms are deeper at all SSTs over the BOB due to weaker stability and
47 mid-tropospheric wind shear. At lower SSTs, the observed high aerosol optical depth (AOD)
48 and low total column water (TCW) over AS results in small cloud effective radius (CER) and
49 weaker reflectivity. As SST increases, AOD decreases and TCW increases leading to large
50 CER and high reflectivity. The changes in these parameters with SST are marginal over the
51 BOB and hence the CER and reflectivity. The predominance of collision-coalescence process
52 below the bright band is responsible for the observed negative slopes in the reflectivity over
53 both the seas. The observed variations in reflectivity are originated at the cloud formation
54 stage over both the seas and these variations are magnified during the descent of
55 hydrometeors to ground.

56

57

58

59

60

61

62

63 **1. Introduction**

64 Indian summer monsoon (ISM - June through September) is one of the most complex
65 weather phenomena, involving coupling between the atmosphere, land and ocean. At the
66 boundary of the ocean and atmosphere air-sea interactions play a key role for the coupled
67 Earth system (Wu and Kirtman 2005; Feng et al. 2018). The sea surface temperature (SST) –
68 precipitation relations are the important measures for the air-sea interactions on different
69 temporal scales (Woolnough et al., 2000; Rajendran et al. 2012). Recent studies (Wang et al.
70 2005; Rajeevan et al. 2012; Chaudhari et al. 2013; 2016; Weller et al. 2016; Feng et al. 2018)
71 have shown that the simulation of ISM can be improved with the exact representation of SST
72 - precipitation relationship. SST modulates the meteorological factors that influence the
73 formation and evolution of different kinds of precipitating systems over tropical oceans
74 (Gadgil et al. 1984; Schumacher and Houze, 2003; Takayabu et al. 2010; Oueslati and Bellon
75 2015).

76 The studies dealing with SST and cloud/precipitation population considered whole
77 Indian Ocean as a single entity (Gadgil et al. 1984; Woolnough et al., 2000; Rajendran et al.
78 2012; Sabin et al. 2012; Meenu et al. 2012; Nair and Rajeev 2014; Roxy 2014). But in reality
79 the Bay of Bengal (BOB) and the Arabian Sea (AS) of Indian Ocean possess distinctly
80 different features (Kumar et al. 2014; Shige et al. 2017; Rajendran et al. 2018; Saikranthi et
81 al. 2019). The monsoon experiment (MONEX) and Bay of Bengal monsoon experiment
82 (BOBMEX) have shown how these two seas are different with respect to each other, in terms
83 of SST, back ground atmosphere and the occurrence of precipitating systems (Krishnamurti
84 1985; Houze and Churchill 1987; Gadgil 2000; Bhat et al. 2001). The SST in the AS cools
85 between 10 °N and 20 °N during the monsoon season whereas warming is seen in other
86 global Oceans between the same latitudes (Krishnamurthi 1981). SST variability is large over
87 the AS than the BOB at seasonal and intraseasonal scales (Sengupta et al. 2001; Roxy et al.

88 2013). The monsoonal winds (in particular the low-level jet) are stronger over the AS than
89 BOB (Findlater 1969). Also, lower-tropospheric thermal inversions are more frequent and
90 stronger over the AS than BOB (Narayanan and Rao 1981; Sathiyamoorthy et al. 2013).
91 Thus, the atmospheric and sea surface conditions and in turn the occurrence of different kinds
92 of precipitating systems are quite different over the BOB and the AS during the ISM period.
93 For instance, long-term measurements of Tropical Rainfall Measuring Mission (TRMM)
94 precipitation radar (PR) have shown that shallow systems are more prevalent over the AS,
95 while deeper systems occur frequently over the BOB (Liu et al. 2007; Romatschke et al.
96 2010; Saikranthi et al. 2014, 2018; Houze et al. 2015).

97 The aforementioned studies mainly focused on the morphology of vertical structure of
98 precipitation, but, none of them studied the variation of vertical structure of precipitation (in
99 terms of occurrence and intensity) with SST and the differences in the vertical structure over
100 AS and BOB. On the other hand, information on the vertical structure of precipitation is
101 essential for improving the accuracy of rainfall estimation (Fu and Liu 2001; Sunilkumar et
102 al. 2015), understanding the dynamical and microphysical processes of hydrometeor
103 growth/decay mechanisms (Houze 2004; Greets and Dejene 2005; Saikranthi et al. 2014; Rao
104 et al. 2016) and for improving the latent heating retrievals (Tao et al. 2006, 2016). SST being
105 the main driving force to trigger precipitating systems through air-sea interactions (Sabin et
106 al. 2012; Nuijens et al. 2017), can alter the vertical structure of precipitation (Oueslati and
107 Bellon 2015). Therefore, the present study aims to understand the variation of vertical
108 structure of precipitation (in terms of precipitation top height and intensity) with SST over the
109 AS and BOB. Besides the SST, vertical structure can be modified by aerosols (or CCN,
110 mostly at the cloud formation stage) and thermodynamics of the ambient atmosphere. For
111 instance, recent studies have shown the impact of surface PM_{10} aerosols in altering the

112 vertical structure of precipitation (Guo et al., 2018). All these parameters, therefore, are
113 considered in the present study to explain the differences in the vertical structure.

114 **2. Data**

115 The present study utilizes 16 years (1998-2013) of TRMM-PR's 2A25 (version 7)
116 dataset, comprising of vertical profiles of attenuation corrected reflectivity (Iguchi et al.
117 2009), during the ISM. The range resolution of TRMM-PR reflectivity profiles is 250 m with
118 a horizontal footprint size of ~4.3 and 5 km before and after the boosting of its orbit from 350
119 km to 403 km, respectively. It scans $\pm 17^\circ$ from nadir with a beam width of 0.71° covering a
120 swath of 215 km (245 km after the boost). The uniqueness of TRMM-PR data is its ability in
121 pigeonholing the precipitating systems into convective, stratiform and shallow rain. This
122 classification is based on two methods namely the horizontal method (H - method) and the
123 vertical method (V - method) (Awaka et al. 2009). The original TRMM-PR 2A25 vertical
124 profiles of attenuation corrected reflectivity are gridded to a three dimensional Cartesian
125 coordinate system with a spatial resolution of $0.05^\circ \times 0.05^\circ$. The detailed methodology of
126 interpolating the TRMM-PR reflectivity data into the 3D Cartesian grid is discussed in Houze
127 et al. (2007). This dataset is available at the University of Washington website
128 (<http://trmm.atmos.washington.edu/>). Profiles are classified as deep (shallow), if their storm
129 top reflectivity ≥ 17 dBZ lies above (1 km below) the 0°C isotherm.

130 To understand the observed variations in the vertical structure of precipitation in the
131 light of microphysics of clouds, Moderate Resolution Imaging Spectroradiometer (MODIS)
132 AQUA satellite level 3 data (MYD08) are considered. In particular, the daily atmospheric
133 products of aerosol optical depth (AOD) (Hubanks et al. 2008) and cloud effective radius
134 (CER) liquid (Platnick et al. 2017) during the period 2003 and 2013 have been used. MODIS
135 AOD dataset is a collection of aerosol optical properties at 550 nm wavelength, as well as
136 particle size information. Level 2 MODIS AOD is derived from radiances using either one of

137 the three different algorithms, i.e., over ocean Remer et al. (2005) algorithm, over land the
 138 Dark-Target (Levy et al. 2007) algorithm and for brighter land surfaces the Deep-Blue (Hsu
 139 et al. 2004) algorithm. CER is nothing but the weighted mean of the size distribution of cloud
 140 drops i.e., the ratio of third moment to second moment of the drop size distribution. In the
 141 level 3 MODIS daily dataset, aerosol and cloud products of level 2 data pixels with valid
 142 retrievals within a calendar day are first aggregated and gridded to a daily average with a
 143 spatial resolution of $1^\circ \times 1^\circ$. For CER grid box values, CER values are weighted by the
 144 respective ice/liquid water cloud pixel counts for the spatiotemporal aggregation and
 145 averaging processes.

146 The background atmospheric structure (winds and total column water) and SST
 147 information are taken from the European Centre for Medium Range Weather Forecasting
 148 (ECMWF) Interim Reanalysis (ERA) (Dee et al. 2011). ERA-Interim runs 4DVAR
 149 assimilation twice daily (00 and 12 UTC) to determine the most likely state of the atmosphere
 150 at a given time (analysis). The consistency across variables in space and time (during 12-hour
 151 intervals) is thus ensured by the atmospheric model and its error characteristics as specified in
 152 the assimilation. ERA-Interim is produced at T255 spectral resolution (about 0.75° , ~ 83 km)
 153 with a temporal resolution of 6h for upper air fields and 3h for surface fields. The original
 154 $0.75^\circ \times 0.75^\circ$ spatial resolution gridded dataset is rescaled to a resolution of $0.125^\circ \times 0.125^\circ$.
 155 The temporal resolution of the dataset used in the present study is 6h (00, 06, 12 and 18
 156 UTC). The equivalent potential temperature (θ_e) is estimated from the ERA-Interim datasets
 157 using the following formula (Wallace and Hobbs 2006):

$$\theta_e = \theta \exp\left(\frac{L_v w_s}{C_p T}\right) \quad (1)$$

158 where θ is the potential temperature, L_v is the latent heat of vaporization, w_s is the saturation
 159 mixing ratio, C_p is the specific heat at constant pressure and T is the absolute temperature.

160 The variation of vertical structure of precipitation with SST are studied by considering
161 the dataset between 63 °E – 72 °E and 8 °N – 20 °N over the AS and 83 °E – 92 °E and 8 °N
162 – 21 °N over the BOB. These regions of interest along with the ISM seasonal mean SST over
163 the two seas are depicted in Fig. 1. These regions are selected in such a way that the costal
164 influence on SST is eluded from the analysis. As the rainfall is scanty over the western AS
165 (west of 63°E latitude) during the ISM (Saikranthi et al. 2018), this region is also not
166 considered in the present analysis. The seasonal mean SST is higher over the BOB than in the
167 AS by more than 1 °C during the ISM season, in agreement with Shenoi et al. (2002). The
168 nearest space and time matched SST data from ERA-Interim are assigned to the TRMM-PR
169 and MODIS observations for further analysis.

170 **3. Variation of vertical structure of precipitation with SST**

171 The occurrence (in terms of %) of conditional precipitation echoes ($Z \geq 17$ dBZ) at
172 different altitudes as a function of SST over the AS and the BOB is shown in Fig. 2. The
173 variation of precipitation echo occurrence frequency with SST is quite different over both the
174 seas. The top of the precipitation echoes extends to higher altitudes with increasing SST over
175 the AS, while such variation is not quite evident over the BOB. Precipitation echoes are
176 confined to < 8 km at lower SST (< 28 °C) over the AS, but exhibits a gradual rise in height
177 with increase in SST. Large population density of precipitation echoes at lower altitudes is
178 mainly due to the abundant occurrence of shallow storms over the AS (Saikranthi et al. 2014,
179 2019; Rao et al. 2016). Interestingly, the occurrence of precipitation echoes is seen at higher
180 altitudes even at lower SSTs over the BOB, indicating the presence of deeper storms. Such
181 systems exist at all SST's over the BOB.

182 To examine the variation of reflectivity profiles with SST, median profiles of
183 reflectivity in each SST bin are computed over the AS and the BOB separately for deep and
184 shallow systems and are depicted in Figs. 3 & 4, respectively. The space- and time-matched

185 conditional reflectivity profiles are grouped into 1°C SST bins and then the median is
186 estimated at each height, only if the number of conditional reflectivity pixels (Figs. 3c; 3f; 4c
187 & 4f) is greater than 500. The median reflectivity profiles corresponding to the deep systems
188 are distinctly different over the AS and the BOB (Figs. 3a & 3d), even at the same SST. Over
189 the AS, reflectivity of deep systems at different SSTs shows small variations (≤ 1 dBZ) above
190 the melting region (> 5 km), but varies significantly (~ 4.5 dBZ) below the melting level (< 5
191 km). These variations in reflectivity profiles with SST are negligible (< 0.5 dBZ) over the
192 BOB both above and below the melting region. The reflectivity increases from ~ 26.5 dBZ to
193 ~ 31 dBZ, with increase in SST from 26°C to 30°C over the AS, but it is almost the same (\sim
194 30 dBZ) at all SST's over the BOB below the melting layer. The standard deviation of
195 reflectivity, representing the variability in reflectivity within the SST bin, is similar at all
196 SSTs over both the seas except for the 26°C SST over AS. At this SST, the standard
197 deviation is lesser by ~ 1 dBZ than that of other SSTs.

198 The median reflectivity profiles of shallow storms depicted in Figs. 4a & 4d also
199 show a gradual increase in reflectivity from 20 dBZ to ~ 22 dBZ as SST changes from 26°C
200 to 31°C at the precipitation top altitude over the AS and don't show any variation with SST
201 over the BOB. However at 1 km altitude, except at 26°C SST over the AS, the reflectivity
202 variation with SST is not substantial over both the seas. The standard deviation of reflectivity
203 profiles show ~ 1 dBZ variation with SST (from 26°C to 31°C) at all altitudes over the AS
204 and don't show any variation over the BOB. The standard deviation of reflectivity for
205 shallow storms varies from 3 to 4 dBZ at the precipitation top altitude and 4.5 to 5.3 dBZ at 1
206 km altitude over the AS while it shows ~ 4 dBZ at precipitation top and ~ 5.5 dBZ at 1 km
207 altitude over the BOB.

208 **4. Factors affecting the vertical structure of precipitation and their variability with SST**

209 The formation and evolution of precipitating systems over oceans depend on
 210 dynamical, thermodynamical and microphysical factors, like SST, wind shear, vertical wind
 211 velocity, stability, CER, etc., and need to be considered for understanding the vertical
 212 structure of precipitation (Li and Min 2010; Creamean et al. 2013; Chen et al. 2015; Shige
 213 and Kummerow 2016; Guo et al 2018).

214 **4.1. Dynamical and thermodynamical factors:**

215 Takahashi and Dado (2018) have shown that zonal wind variations can also explain
 216 some variability of rain. To examine the impact of zonal wind on rainfall over the Arabian
 217 Sea and Bay of Bengal, the data are segregated into 3 wind regimes as weak (monsoon
 218 westerlies lies between 0 and 6 m s⁻¹), moderate (monsoon westerlies lies between 6 to 12 m
 219 s⁻¹) and strong (monsoon westerlies > 12 m s⁻¹) winds. The median vertical profiles of
 220 reflectivity are computed for each SST bin corresponding to deep and shallow systems (not
 221 shown here). Two important observations are noted from these figures. 1) Vertical profiles of
 222 reflectivity show considerable variation (2-5 dBZ) in all wind categories over the Arabian
 223 Sea, but such variations are absent over the Bay of Bengal. It implies that the reported
 224 differences in reflectivity profiles over the Arabian Sea and Bay of Bengal exist in all wind
 225 regimes. 2) The variation in reflectivity with SST increases with weak to strong wind regime
 226 over the Arabian Sea, indicating some influence of wind on reflectivity (rainfall) variation.

227 To understand the role of stability/instability, θ_e values computed from (1) using the
 228 ERA-Interim datasets during the ISM period over the AS and the BOB are averaged for a
 229 season and are depicted in Figs. 5(a) & 5(b), respectively. The surface θ_e (at 1000 hPa) values
 230 are larger over the BOB than those over AS for the same SST, indicating that the instability
 231 and convective available potential energy (CAPE) could be higher over the BOB. Indeed,
 232 higher CAPE is seen over the BOB (Fig. S1, calculated following Emanuel 1994) than AS at
 233 all SSTs by a magnitude > 300 J kg⁻¹. The θ_e increases with SST from 358 °K to 368 °K

234 from 27 °C to 31 °C and from 350 °K to 363 °K from 26 °C to 31 °C over the BOB and the
235 AS, respectively. The CAPE also increases with rise in SST over both the seas. To know the
236 stability of the atmosphere θ_e gradients are considered. Irrespective of SST, positive gradients
237 in θ_e are observed between 900 and 800 hPa levels over the AS indicating the presence of
238 strong stable layers. The strength of these stable layers decreases with increasing SST. These
239 stable layers are formed mainly due to the flow of continental dry warm air from Arabian
240 Desert and Africa above the maritime air causing temperature inversions below 750 hPa level
241 over the AS during the ISM period (Narayanan and Rao 1981). However over the BOB, such
242 temperature inversions are not seen in the lower troposphere.

243 To understand the effect of wind field on the vertical structure of precipitation,
244 profiles of ISM seasonal mean vertical wind velocity and vertical shear in horizontal wind at
245 various SSTs over the AS and the BOB are shown in Figs. 5(c), 5(d) & 5(e), 5(f)
246 respectively. The updrafts are prevalent at all SSTs throughout the troposphere over the BOB,
247 whereas downdrafts are seen in the mid-troposphere (between 200 and 600 hPa levels) up to
248 27 °C and updrafts in the entire troposphere at higher SSTs over the AS. Also, the magnitude
249 of the vertical wind velocity varies significantly with SST in the mid-troposphere over the
250 AS. Over the BOB, the magnitude of updrafts increases with altitude in the lower and middle
251 troposphere, but doesn't vary much with SST. In the mid-troposphere, updrafts are stronger
252 by $> 0.02 \text{ Pa s}^{-1}$ over the BOB than over the AS. The profiles shown in Fig. 5(e) & 5(f) are
253 the mean vertical shear in horizontal wind estimated following Chen et al. (2015) at different
254 levels with reference to 950 hPa level. The wind shear increases with increasing altitude at all
255 the SSTs up to 400 hPa, but the rate of increase is distinctly different between the AS and the
256 BOB at SSTs less than 28 °C and nearly the same at higher SSTs. The wind shear decreases
257 systematically with SST ($\sim 1.5 \text{ m s}^{-1}$ for 1° increase in SST) in the middle troposphere over
258 the AS while the change is minimal over the BOB ($\sim 2 \text{ m s}^{-1}$ for 27 °C and 31 °C).

259 Chen et al. (2015) highlighted the importance of mid-tropospheric wind shear in
260 generating mesoscale local circulations, like low-level cyclonic and upper-level anticyclonic
261 circulations. This feature is apparent over the AS, where down drafts are prevalent in mid-
262 upper troposphere and updrafts in the lower troposphere at lower SSTs. As SST increases, the
263 wind shear decreases and the updraft increases in the mid-troposphere. However, over the
264 BOB the wind shear is relatively weak when compared to the AS and hence the updrafts are
265 seen up to 200 hPa level at all SSTs. The weaker CAPE and stable mid-troposphere coupled
266 with upper- to mid- tropospheric downdrafts at lower SSTs over the AS inhibit the growth of
267 precipitating systems to higher altitudes and in turn precipitate in the form of shallow rain.
268 This result is in accordance with the findings of Shige and Kummerow (2016) that showed
269 the static stability at lower levels inhibits the growth of clouds and promotes the detrainment
270 of clouds over the Asian monsoon region and is considered as an important parameter in
271 determining the precipitation top height. As SST increases large CAPE and updrafts in the
272 middle troposphere collectively support the precipitating systems to grow to higher altitudes,
273 as evidenced in Fig. 2a. On the other hand, large CAPE and updrafts in the middle
274 troposphere prevalent over the BOB at all SSTs are conducive for the precipitating systems to
275 grow to higher altitudes as seen in Fig. 2b.

276 **4.2. Microphysical factors**

277 The observed differences in reflectivity profiles of precipitation with SST could be
278 originated at the cloud formation stage itself or manifested during the evolution stage or due
279 to both. Information on AOD and CER would be ideal to infer microphysical processes at the
280 cloud formation stage. CER values are mainly controlled by the ambient aerosols
281 concentration and the available moisture (Twomey 1977; Albrecht 1989; Tao et al. 2012; and
282 Rosenfeld et al. 2014). For fixed liquid water content, as the concentration of aerosols
283 increases, the number of cloud drops increases and CER decreases (Twomey 1977). To

284 understand the variation of AOD and total column water (TCW) and the resultant CER with
285 SST, the mean AOD and TCW for different SST bins are plotted in Figs. 6a & 6b. The mean
286 and standard error are calculated only when the number of data points is more than 100 in
287 each SST bin. AOD decreases from 0.62 to 0.31 with rise in SST from 26 °C to 31 °C over
288 the AS but only from 0.42 to 0.36 as SST varies from 27 °C to 30 °C and then increases at
289 higher SSTs over the BOB. The variation of TCW with SST (Fig. 6b) shows a gradual
290 increase with SST over the AS while it decreases initially from 27°C to 28°C, and then
291 increases over the BOB. At a given SST the TCW is more in the BOB (> 8 mm) than in the
292 AS.

293 The decrease in AOD and an increase in TCW with SST result in an increase in CER
294 (14.7 μm to 20.8 μm from 26°C to 31°C) over the AS (Fig. 7). On the other hand, CER
295 doesn't show much variation with SST (18.5 μm to 19.5 μm from 27°C to 31°C) over BOB
296 due to smaller variations in AOD and TCW. This also shows that the cloud droplets are
297 smaller in size at lower SSTs over the AS than BOB, while they are bigger and nearly equal
298 in size at higher SSTs. Since, reflectivity is more sensitive to the precipitating particle size (Z
299 $\propto D^6$), the smaller-sized hydrometeors at lower SSTs over the AS yield weaker reflectivity
300 than over the BOB (both for deep and shallow systems). As the SST increases, CER as well
301 as the reflectivity increases over the AS. At higher SSTs, the CER values are approximately
302 equal over both the seas and in turn the observed reflectivities (Figs. 3a & 4a). This suggests
303 that the variations seen in the reflectivity are originated in the cloud formation stage itself.

304 The hydrometeors also evolve during their descent to the ground due to several
305 microphysical processes. These processes can be inferred from the vertical structure of
306 precipitation or vertical profiles of reflectivity. The median reflectivity profiles of deep
307 systems show a gradual increase from ~ 10 km to 6 km and an abrupt enhancement is seen
308 just below 6 km over both the seas (Figs. 3a & 3d). The sudden enhancement at the freezing

309 level (radar bright band) is primarily due to the aggregation of hydrometeors, change in
310 dielectric factor from ice to water and change in fall speed from ice hydrometers to raindrops
311 (Fabry and Zawadzki 1995; Rao et al. 2008; Cao et al. 2013). Below the bright band,
312 raindrops grow by collision-coalescence process and reduce their size by either breakup
313 and/or evaporation processes. The collision-coalescence results in negative slope in the
314 reflectivity profile, whereas breakup and evaporation results in positive slope (Liu and Zipser
315 2013; Cao et al. 2013; Saikranthi et al. 2014; Rao et al. 2016). The observed negative slope
316 ($\sim -0.3 \text{ dBZ km}^{-1}$) in the median reflectivity profiles below the bright band indicates
317 dominance of low-level hydrometeor growth over both the seas. The magnitude of the slope
318 decreases with SST over the AS, while it is nearly equal at all SSTs over the BOB. It
319 indicates the growth rate decreases with SST over the AS and remains the same at all SSTs
320 over the BOB. The median reflectivity profiles of shallow systems also show negative slopes
321 ($\sim -1 \text{ dBZ km}^{-1}$) at all SSTs representing the predominance of low-level hydrometeor growth
322 by collision-coalescence processes over both the seas.

323 The present analysis shows that the observed reflectivity changes with SST over both
324 the seas originate at the cloud formation stage and magnify further during the descent of
325 hydrometeors to ground.

326 **5. Conclusions**

327 Sixteen years of TRMM-PR 2A25 reflectivity profiles and 11 years of MODIS AOD
328 and CER data are utilized to understand the differences in variation of vertical structure of
329 precipitation with SST over AS and BOB. Precipitation top height increases with SST over
330 the AS indicating that systems grow to higher altitudes with increase in SST while it is almost
331 same at all SSTs representing that the systems are deeper over the BOB. The decrease in
332 stability and mid-tropospheric wind shear with SST over the AS favour the formation of
333 deeper system at higher systems. However the low stability and small wind shear at all SSTs

334 over the BOB help the formation of deeper systems. The variation of reflectivity with SST is
335 found to be remarkable over the AS and marginal over the BOB. The reflectivity increases
336 with rise in SST over the AS and remains the same at all SSTs over the BOB. This change in
337 reflectivity over the AS is more prominent below the freezing level height (~ 4 dBZ) than the
338 above (~ 1 dBZ). Over the AS, the abundance of aerosols and less moisture at SSTs $< 27^\circ\text{C}$
339 result in high concentration of smaller cloud droplets. As SST increases the aerosol
340 concentration decreases and moisture increases leading to the formation of bigger cloud
341 droplets. Thus, the reflectivity increases with rise in SST over the AS. On the other hand,
342 AOD, TCW and CER do not show substantial variation with SST over the BOB and hence
343 the change in reflectivity is small. Over the BOB, the mid troposphere is wet and
344 hydrometeor's size at the formation stage is nearly the same at all SSTs. The evolution of
345 hydrometeors during their descent is also similar at all SST's. The collision-coalescence
346 process is predominant below the bright band region over both the seas and is responsible for
347 the observed negative slope in the reflectivity profiles.

348 **Author contribution**

349 Kadiri Saikranthi conceived the idea. Kadiri Saikranthi and Basivi Radhakrishna designed the
350 analysis, plotted the figures and wrote the manuscript. Thota Narayana Rao and Sreedharan
351 Krishnakumari Satheesh contributed in discussions as well as in improving the quality of the
352 manuscript.

353 **Acknowledgements**

354 The authors would like to thank Prof. Robert Houze and his team for the interpolated 3D
355 gridded TRMM-PR dataset (<http://trmm.atmos.washington.edu>), ECMWF (<http://data-portal.ecmwf.int/>) team for providing the ERA-Interim dataset and MODIS
356 (<https://ladsweb.modaps.eosdis.nasa.gov/>) science team for providing the AOD and CER
357 dataset. The authors express their gratitude to Prof. J. Srinivasan for his fruitful discussions
358

359 and valuable suggestions in improving the quality of the manuscript. The corresponding
360 author would like to thank Department of Science & Technology (DST), India for providing
361 the financial support through the reference number DST/INSPIRE/04/2017/001185. We
362 thank the anonymous referees for their critical comments in improving the quality of the
363 manuscript.

364

365

366

367

368

369

370

371

372

373

374

375

376

377

378

379

380

381

382

383

384

385

386

387

References

- 388
389 Albrecht, B.A.: Aerosols, cloud microphysics, and fractional cloudiness, *Science*, 245, 1227–
390 1230, 1989.
- 391 Awaka, J., Iguchi, T., and Okamoto, K.: TRMM PR standard algorithm 2A23 and its
392 performance on bright band detection, *J. Meteorol. Soc. Jpn.*, 87A, 31–52, 2009.
- 393 Bhat, G. S., Gadgil, S., Kumar, P. V. H., Kalsi, S. R., Madhusoodanan, P., Murty, V. S., Rao,
394 C. V. P., Babu, V. R., Rao, L.V., Rao, R. R., Ravichandran, M., Reddy, K.G., Rao, P.
395 S., Sengupta, D., Sikka, D. R., Swain, J., and Vinayachandran, P. N.: BOBMEX: The
396 Bay of Bengal Monsoon Experiment, *Bull. Amer. Meteor. Soc.*, 82, 2217–2244, 2001.
- 397 Cao, Q., Hong, Y., Gourley, J. J., Qi, Y., Zhang, J., Wen, Y., and Kirstetter, P. E.: Statistical
398 and physical analysis of the vertical structure of precipitation in the mountainous west
399 region of the United States using 11+ years of space borne observations from TRMM
400 precipitation radar, *J. Appl. Meteorol. Climatol.*, 52, 408-424, 2013.
- 401 Chaudhari, H. S., Pokhrel, S., Kulkarni, A., Hazra, A., and Saha, S. K.: Clouds-SST
402 relationship and interannual variability modes of Indian summer monsoon in the
403 context of clouds and SSTs: observational and modelling aspects, *Int. J. Climatol.*, doi:
404 10.1002/joc.4664, 2016.
- 405 Chaudhari, H. S., Pokhrel, S., Mohanty, S., and Saha, S. K.: Seasonal prediction of Indian
406 summer monsoon in NCEP coupled and uncoupled model, *Theor. Appl. Climatol.*, 114,
407 459–477, doi:10.1007/s00704-013-0854-8, 2013.
- 408 Chen, Q., Fan, J., Hagos, S., Gustafson Jr., W. I., and Berg, L. K.: Roles of wind shear at
409 different vertical levels: Cloud system organization and properties, *J. Geophys. Res.*
410 *Atmos.*, 120, 6551–6574, 2015.
- 411 Creamean, J. M., Suski, K. J., Rosenfeld, D., Cazorla, A., DeMott, P. J., Sullivan, R. C.,
412 White, A. B., Ralph, F. M., Minnis, P., Comstock, J. M., Tomlinson, J. M., Kimberly

- 413 A., and Prather, K. A.: Dust and biological aerosols from the Sahara and Asia influence
414 precipitation in the western U.S., *Science*, 339, 1572–1578,
415 doi:10.1126/science.1227279, 2013.
- 416 Dee, D. P., et al.: The ERA-Interim reanalysis: Configuration and performance of the data
417 assimilation system, *Q. J. R. Meteorol. Soc.*, 137, 553–597, 2011.
- 418 Emanuel, K. A.: Atmospheric convection. Oxford University Press, Oxford, 1994.
- 419 Fabry, F., and Zawadzki, I.: Long-term radar observations of the melting layer of
420 precipitation and their interpretation, *J. Atmos. Sci.*, 52, 838–851, 1995.
- 421 Feng, X., Haines, K., Liu, C., de Boissésón, E., and Polo, I., Improved SST-precipitation
422 intraseasonal relationships in the ECMWF coupled climate reanalysis, *Geophys. Res.
423 Lett.*, 45, 3664–3672, 2018.
- 424 Findlater, J.: A major low-level air current near the Indian Ocean during the northern
425 summer, *Q. J. R. Meteorol. Soc.*, 95, 362–380, 1969.
- 426 Fu, Y., and Liu, G.: The variability of tropical precipitation profiles and its impact on
427 microwave brightness temperatures as inferred from TRMM data, *J. Appl. Meteorol.*,
428 40, 2130–2143, 2001.
- 429 Gadgil, S., Joseph, P. V., and Joshi, N. V.: Ocean atmosphere coupling over monsoonal
430 regions, *Nature*, 312, 141–143, 1984.
- 431 Gadgil, S.: Monsoon–ocean coupling. *Current Sci.*, 78, 309–323, 2000.
- 432 Geerts, B., and Dejene, T.: Regional and diurnal variability of the vertical structure of
433 precipitation systems in Africa based on space borne radar data, *J. Clim.*, 18, 893–916,
434 2005.
- 435 Guo, J., Liu, H., Li, Z., Rosenfeld, D., Jiang, M., Xu, W., Jiang, J. H., He, J., Chen, D., Min,
436 M., and Zhai, P.: Aerosol-induced changes in the vertical structure of precipitation: a
437 perspective of TRMM precipitation radar, *Atmos. Chem. Phys.*, 18, 13329–13343,

- 438 <https://doi.org/10.5194/acp-18-13329-2018>, 2018.
- 439 Houze, R. A., and Churchill, D. D.: Mesoscale organization and cloud microphysics in a Bay
440 of Bengal depression, *J. Atmos. Sci.*, 44, 1845–1867, 1987.
- 441 Houze, R. A., Rasmussen, K. L., Zuluaga, M. D., and Brodzik, S. R.: The variable nature of
442 convection in the tropics and subtropics: A legacy of 16 years of the Tropical rainfall
443 measuring mission satellite, *Rev. Geophys.*, 53, 994–1021, 2015.
- 444 Houze, R. A., Wilton, D. C., and Smull, B. F.: Monsoon convection in the Himalayan region
445 as seen by the TRMM precipitation radar, *Q. J. R. Meteorol. Soc.*, 133, 1389-1411,
446 2007.
- 447 Houze, R. A.: Mesoscale convective systems, *Rev. Geophys.*, 42, RG4003, doi:
448 10.1029/2004RG000150, 2004.
- 449 Hsu, N., Tsay, S., King, M., and Herman, J.: Aerosol properties over bright-reflecting source
450 regions, *Geosci. Remote Sens. IEEE Trans.*, 42, 557–569, 2004.
- 451 Hubanks, P., King, M., Platnick, S., and Pincus, R.: MODIS atmosphere L3 gridded product
452 algorithm theoretical basis document collection 005 Version 1.1, Tech. Rep. ATBD-
453 MOD-30, NASA, 2008.
- 454 Iguchi, T., Kozu, T., Kwiatkowski, J., Meneghini, R., Awaka, J., and Okamoto, K.:
455 Uncertainties in the rain profiling algorithm for the TRMM precipitation radar, *J.*
456 *Meteor. Soc. Japan*, 87A, 1–30, doi:10.2151/jmsj.87A.1, 2009.
- 457 Krishnamurti, T. N.: Summer monsoon experiment – A review. *Mon. Wea. Rev.*, 113, 1590-
458 1626, 1985.
- 459 Krishnamurti, T.: Cooling of the Arabian Sea and the onset-vortex during 1979. Recent
460 progress in equatorial oceanography: A report of the final meeting of SCOR
461 WORKING GROUP 47 in Venice, Italy, 1-12, 1981. [Available from Nova Univ.,
462 Ocean Science Center, Dania, FL 33004].

- 463 Kumar, S., Hazra, A., and Goswami, B. N.: Role of interaction between dynamics,
464 thermodynamics and cloud microphysics on summer monsoon precipitating clouds over
465 the Myanmar coast and the Western Ghats, *Clim. Dyn.*, 43, 911–924,
466 doi:10.1007/s00382-013-1909-3, 2014.
- 467 Levy, R., Remer, L., Mattoo, S., Vermote, E., and Kaufman, Y.: Second-generation
468 operational algorithm: Retrieval of aerosol properties over land from inversion of
469 moderate resolution imaging spectroradiometer spectral reflectance, *J. Geophys. Res.*,
470 112, D13, doi:10.1029/2006JD007811, 2007.
- 471 Li, R., and Min, Q.-L.: Impacts of mineral dust on the vertical structure of precipitation, *J.*
472 *Geophys. Res.*, 115, D09203, doi:10.1029/2009JD011925, 2010.
- 473 Liu, C., Zipser, E., and Nesbitt, S. W.: Global distribution of tropical deep convection:
474 Different perspectives using infrared and radar as the primary data source, *J. Climate*,
475 20, 489-503, 2007.
- 476 Liu, C., and Zipser, E. J.: Why does radar reflectivity tend to increase downward toward the
477 ocean surface, but decrease downward toward the land surface?, *J. Geophys. Res.*
478 *Atmos.*, 118, 135-148, doi: 10.1029/2012JD018134, 2013.
- 479 Meenu, S., Parameswaran, K., and Rajeev, K.: Role of sea surface temperature and wind
480 convergence in regulating convection over the tropical Indian Ocean, *J. Geophys. Res.*
481 *Atmos.*, 117, D14102, 2012.
- 482 Nair, A. K. M., and Rajeev, K.: Multiyear CloudSat and CALIPSO observations of the
483 dependence of cloud vertical distribution on sea surface temperature and tropospheric
484 dynamics, *J. Clim.*, 27, 672–683, doi:10.1175/JCLI-D-13-00062.1, 2014.
- 485 Narayanan, M. S., and Rao, B. M.: Detection of monsoon inversion by TIROS-N satellite,
486 *Nature*, 294, 546-548, 1981.
- 487 Nuijens, L., Emanuel, K., Masunaga, H., and L'Ecuyer, T.: Implications of warm rain in

- 488 shallow cumulus and congestus clouds for large-scale circulations, *Surv. Geophys.*, 38,
489 1257-1282, 2017.
- 490 Oueslati, B., and Bellon, G.: The double ITCZ bias in CMIP5 models: interaction between
491 SST, large-scale circulation and precipitation. *Clim. Dyn.*, 44, 585-607, 2015.
- 492 Platnick, S., et al.: The MODIS cloud optical and microphysical products: Collection 6
493 updates and examples from Terra and Aqua, *IEEE Trans. Geosci. Remote Sens.*, 55,
494 502–525, doi:10.1109/TGRS.2016.2610522, 2017.
- 495 Rajeevan, M., Unnikrishnan, C. K., and Preethi, B.: Evaluation of the ENSEMBLES multi-
496 model seasonal forecasts of Indian summer monsoon variability, *Clim. Dyn.*, 38, 2257–
497 2274, 2012.
- 498 Rajendran, K., Nanjundiah, R. S., Gadgil, S., and Srinivasan, J.: How good are the
499 simulations of tropical SST–rainfall relationship by IPCC AR4 atmospheric and
500 coupled models?, *J. Earth Sys. Sci.*, 121(3), 595–610, 2012.
- 501 Rajendran, K., Gadgil, S. and Surendran, S.: Monsoon season local control on precipitation
502 over warm tropical oceans, *Meteorol. Atmos. Phys.*, doi:10.1007/s00703-018-0649-7,
503 2018.
- 504 Rao, T. N., Kirankumar, N. V. P., Radhakrishna, B., Rao, D. N., and Nakamura, K.:
505 Classification of tropical precipitating systems using wind profiler spectral moments.
506 Part I: Algorithm description and validation, *J. Atmos. Oceanic Technol.*, 25, 884–897,
507 2008.
- 508 Rao, T. N., Saikranthi, K., Radhakrisna, B., and Rao, S. V. B.: Differences in the
509 climatological characteristics of precipitation between active and break spells of the
510 Indian summer monsoon, *J. Clim.*, 29, 7797-7814, 2016.

- 511 Remer, L., Kaufman, Y., Tanré, D., Mattoo, S., Chu, D., Martins, J., Li, R., Ichoku, C.,
512 Levy, R., Kleidman, R., Eck, T., Vermote, E., and Holben, B.: The MODIS aerosol
513 algorithm, products, and validation, *J. Atmos. Sci.*, 62, 947–973, 2005.
- 514 Romatschke, U., Medina, S., and Houze, R. A.: Regional, seasonal, and diurnal variations of
515 extreme convection in the South Asian region, *J. Clim.*, 23, 419–439, 2010.
- 516 Rosenfeld, D., et al.: Global observations of aerosol-cloud-precipitation-climate interactions,
517 *Rev. Geophys.*, 52, 750-808, doi:10.1002/2013RG000441, 2014.
- 518 Roxy, M., Tanimoto, Y., Preethi, B., Terray, P., and Krishnan, R.: Intraseasonal SST-
519 precipitation relationship and its spatial variability over the tropical summer monsoon
520 region, *Clim. Dyn.*, 41, 45-61, 2013.
- 521 Roxy, M.: Sensitivity of precipitation to sea surface temperature over the tropical summer
522 monsoon region—and its quantification, *Clim. Dyn.*, 43, 1159-1169, 2014.
- 523 Sabin, T., Babu, C., and Joseph, P.: SST–convection relation over tropical oceans, *Int. J.*
524 *Climatol.* 33, 1424–1435, 2012.
- 525 Saikranthi, K., Radhakrishna, B., Satheesh, S. K., and Rao, T. N.: Spatial variation of
526 different rain systems during El Niño and La Niña periods over India and adjoining
527 ocean, *Clim. Dyn.*, 50, 3671-3685, doi: 10.1007/s00382-017-3833-4, 2018.
- 528 Saikranthi, K., Rao, T. N., Radhakrishna, B., and Rao, S. V. B.: Morphology of the vertical
529 structure of precipitation over India and adjoining oceans based on long-term
530 measurements of TRMMPR, *J. Geophys. Res. Atmos.*, 119, 8433–8449, doi:
531 10.1002/2014JD021774, 2014.
- 532 Saikranthi, K., Radhakrishna, B., Rao, T. N., and Satheesh, S. K.: Differences in the
533 association of sea surface temperature - precipitating systems over the Bay of Bengal
534 and the Arabian Sea during southwest monsoon season. *Int. J. Climatol.*,
535 doi:10.1002/joc.6074, 2019.

- 536 Sathiyamoorthy, V., Mahesh, C., Gopalan, K., Prakash, S., Shukla, B. P., Mathur, A.:
537 Characteristics of low clouds over the Arabian Sea, *J. Geophys. Res. Atmos.*, 118,
538 13489-13503, 2013.
- 539 Schumacher, C. and Houze, R. A.: Stratiform rain in the tropics as seen by the TRMM
540 precipitation radar, *J. Climate.*, 16, 1739–1756, 2003.
- 541 Sengupta, D., Goswami, B. N., and Senan, R.: Coherent intraseasonal oscillations of ocean
542 and atmosphere during the Asian summer monsoon, *Geophys. Res. Lett.*, 28, 4127–
543 4130, 2001.
- 544 Shenoi, S. S. C., Shankar, D., and Shetye, S. R.: Differences in heat budgets of the near-
545 surface Arabian Sea and Bay of Bengal: Implications for the summer monsoon, *J.*
546 *Geophys. Res.*, 107(C6), 3052, doi:10.1029/2000JC000679, 2002.
- 547 Shige, S. and Kummerow, C.D.: Precipitation-Top Heights of Heavy Orographic Rainfall in
548 the Asian Monsoon Region, *J. Atmos. Sci.*, 73, 3009–3024, 2016.
- 549 Shige, S., Nakano, Y., and Yamamoto, M. K.: Role of orography, diurnal cycle, and
550 intraseasonal oscillation in summer monsoon rainfall over Western Ghats and Myanmar
551 coast, *J. Climate*, 30, 9365–9381, doi:10.1175/JCLI-D-16-0858.1, 2017.
- 552 Sunilkumar, K., Rao, T. N., Saikranthi, K., and Rao, M. P.: comprehensive evaluation of
553 multisatellite precipitation estimates over India using gridded rainfall data, *J. Geophys.*
554 *Res. Atmos.*, 120, doi:10.1002/2015JD023437, 2015.
- 555 Takahashi, H. G., and Dado, J. M. B.: Relationship between sea surface temperature and
556 rainfall in the Philippines during the Asian summer monsoon, *J. Meteor. Soc. Japan.*,
557 96 (3), 283–290, doi:10.2151/jmsj.2018-03, 2018.
- 558 Takayabu, Y. N., Shige, S., Tao, W., and Hirota, N.: Shallow and deep latent heating modes
559 over tropical Oceans observed with TRMM PR spectral latent heating Data, *J. Climate*,
560 23, 2030–2046, 2010.

- 561 Tao, W.-K., Chen, J.-P., Li, Z., Wang, C., and Zhang, C.: Impact of aerosols on convective
562 clouds and precipitation, *Rev. Geophys.*, 50, RG2001, doi:10.1029/2011RG000369,
563 2012.
- 564 Tao, W.-K., et al.: Retrieval of latent heating from TRMM measurements, *Bull. Am.*
565 *Meteorol. Soc.*, 87, 1555–1572, 2006.
- 566 Tao, W.-K., et al.: TRMM latent heating retrieval: Applications and comparisons with field
567 campaigns and large-scale analyses, *Meteorological Monographs - Multi-scale*
568 *Convection-Coupled Systems in the Tropics: A tribute to Dr. Michio Yanai*, 56, 2.1-
569 2.34, doi:10.1175/AMSMONOGRAPHS-D-15-0013.1, 2016.
- 570 Twomey, S.: The influence of pollution on the short wave albedo of clouds, *J. Atmos. Sci.*,
571 34, 1149–1152, 1977.
- 572 Wallace, J. M., and Hobbs, P. V.: Atmospheric science: An introductory survey, Second
573 edition, Academic press, pp. 85, 2006.
- 574 Wang, B., Ding, Q., Fu, X., Kang, I.-S., Jin, K., Shukla, J., and Doblas-Reyes, F.:
575 Fundamental challenge in simulation and prediction of summer monsoon rainfall,
576 *Geophys. Res. Lett.*, 32, L15711, doi:10.1029/2005GL022734, 2005.
- 577 Weller, R. A., Farrar, J. T., Buckley, J., Mathew, S., Venkatesan, R., Lekha, J. S., Chaudhuri,
578 D., Kumar, N. S., and Kumar, B. P.: Air-sea interaction in the Bay of Bengal,
579 *Oceanography*, 29(2), 28–37, 2016.
- 580 Woolnough, S.J., Slingo, J.M., and Hoskins, B.J.: The relationship between convection and
581 sea surface temperature on intraseasonal timescales, *J. Climate*, 13, 2086–2104, 2000.
- 582 Wu, R., and Kirtman, B. P.: Roles of Indian and Pacific Ocean air–sea coupling in tropical
583 atmospheric variability, *Clim. Dyn.*, 25(2–3), 155–170, 2005.
- 584
- 585

586
587
588
589
590
591
592
593
594
595
596
597
598
599
600
601
602
603
604
605
606
607
608
609
610
611

Figure captions

Figure 1: Spatial distribution of ISM mean SST (in °C) obtained from ERA-Interim reanalysis data over the AS (63°E-72°E & 8°N-20°N) and the BOB (83°E-92°E & 8°N-21°N). The regions considered in this analysis over these two seas are shown with the boxes.

Figure 2: (a) and (b) represent the altitudinal distribution of occurrence of conditional reflectivity (≥ 17 dBZ) as a function of SST with respect to precipitation occurrence at that particular SST interval over the AS and the BOB, respectively.

Figure 3: (a), (d) and (b), (e) represent vertical profiles of median reflectivity correspond to deep systems and their standard deviation (in dBZ) with SST over the AS and the BOB, respectively during the ISM season. (c) and (f) show the number of conditional reflectivity pixels at each altitude used for the estimation of the median and standard deviation.

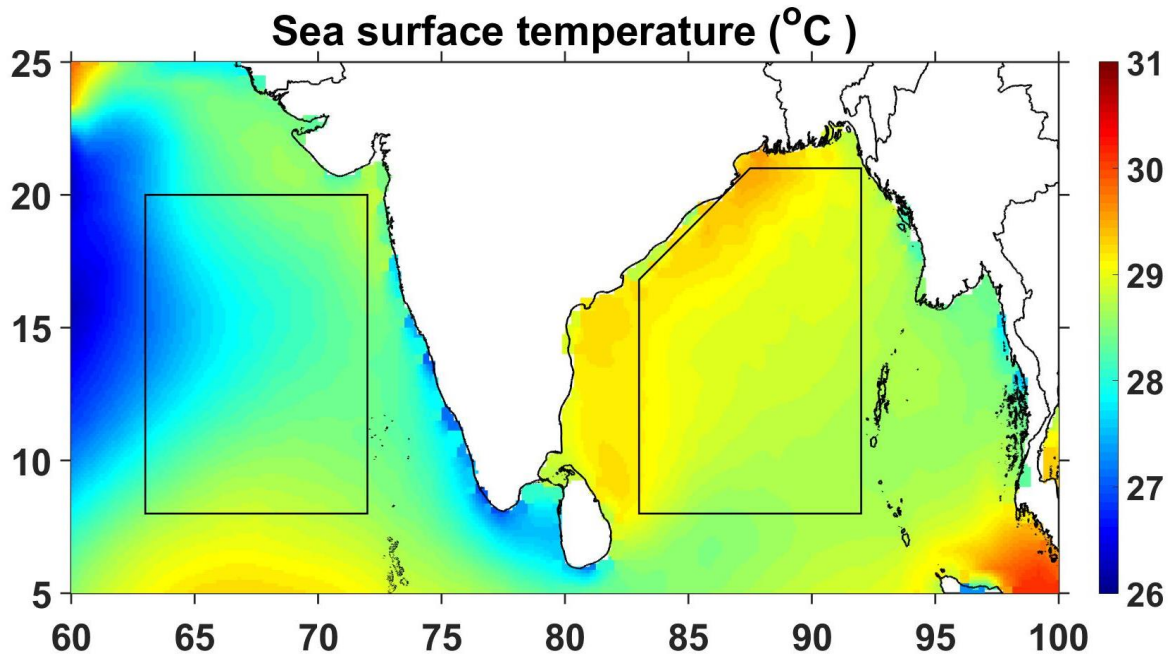
Figure 4: Same as Fig. 3 but for shallow precipitating systems.

Figure 5: (a) and (b), respectively, represent the vertical profiles of mean θ_e (in K) with SST over the AS and the BOB during the ISM season. (c) and (d) and (e) and (f) are same as (a) and (b) but for mean vertical velocity (in Pa s^{-1}) and wind gradient with reference to 950 hPa level (in m s^{-1}).

Figure 6: (a) Mean and standard error of AOD and (b) TCW (in kg m^{-2}) with SST over the AS and the BOB during ISM.

Figure 7: Variation of mean and standard error of CER liquid (in μm) with SST over the AS and the BOB during the ISM season.

Figures



614

615 **Figure 1:** Spatial distribution of ISM mean SST (in °C) obtained from ERA-Interim
616 reanalysis data over the AS (63°E-72°E & 8°N-20°N) and the BOB (83°E-92°E &
617 8°N-21°N). The regions considered in this analysis over these two seas are shown
618 with the boxes.

619

620

621

622

623

624

625

626

627

628

629

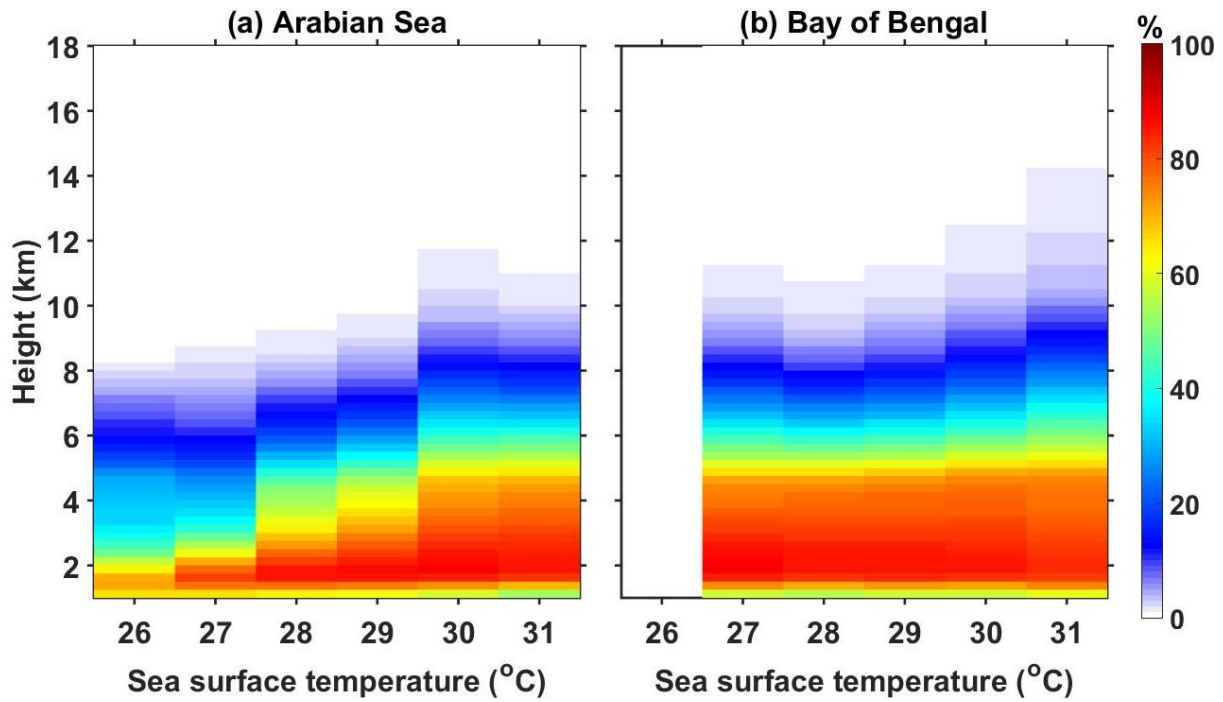
630

631

632

633

634



635

636

637 **Figure 2:** (a) and (b) represent the altitudinal distribution of occurrence of conditional
 638 reflectivity (≥ 17 dBZ) as a function of SST with respect to precipitation occurrence at
 639 that particular SST interval over the AS and the BOB, respectively.

640

641

642

643

644

645

646

647

648

649

650

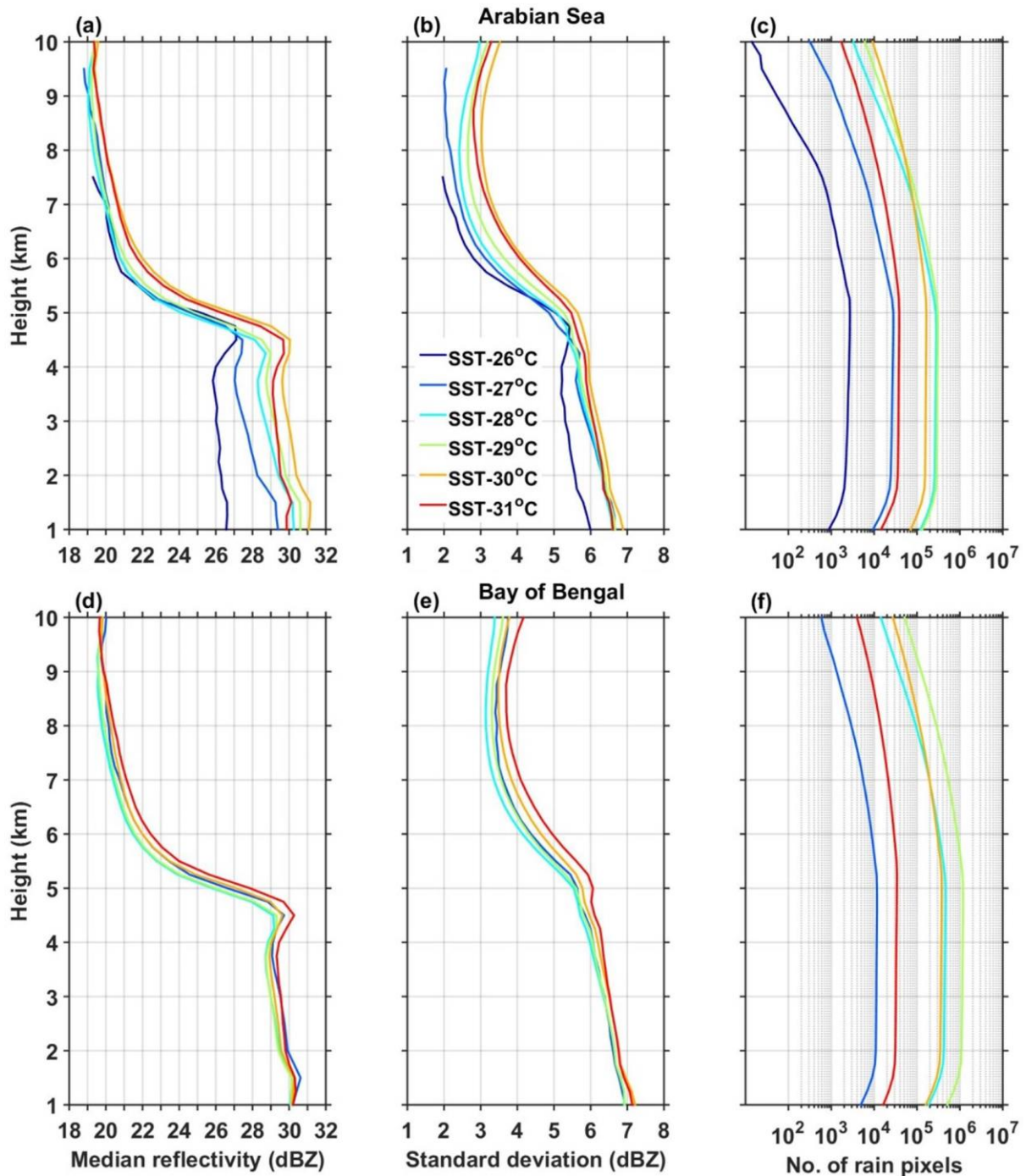
651

652

653

654

655



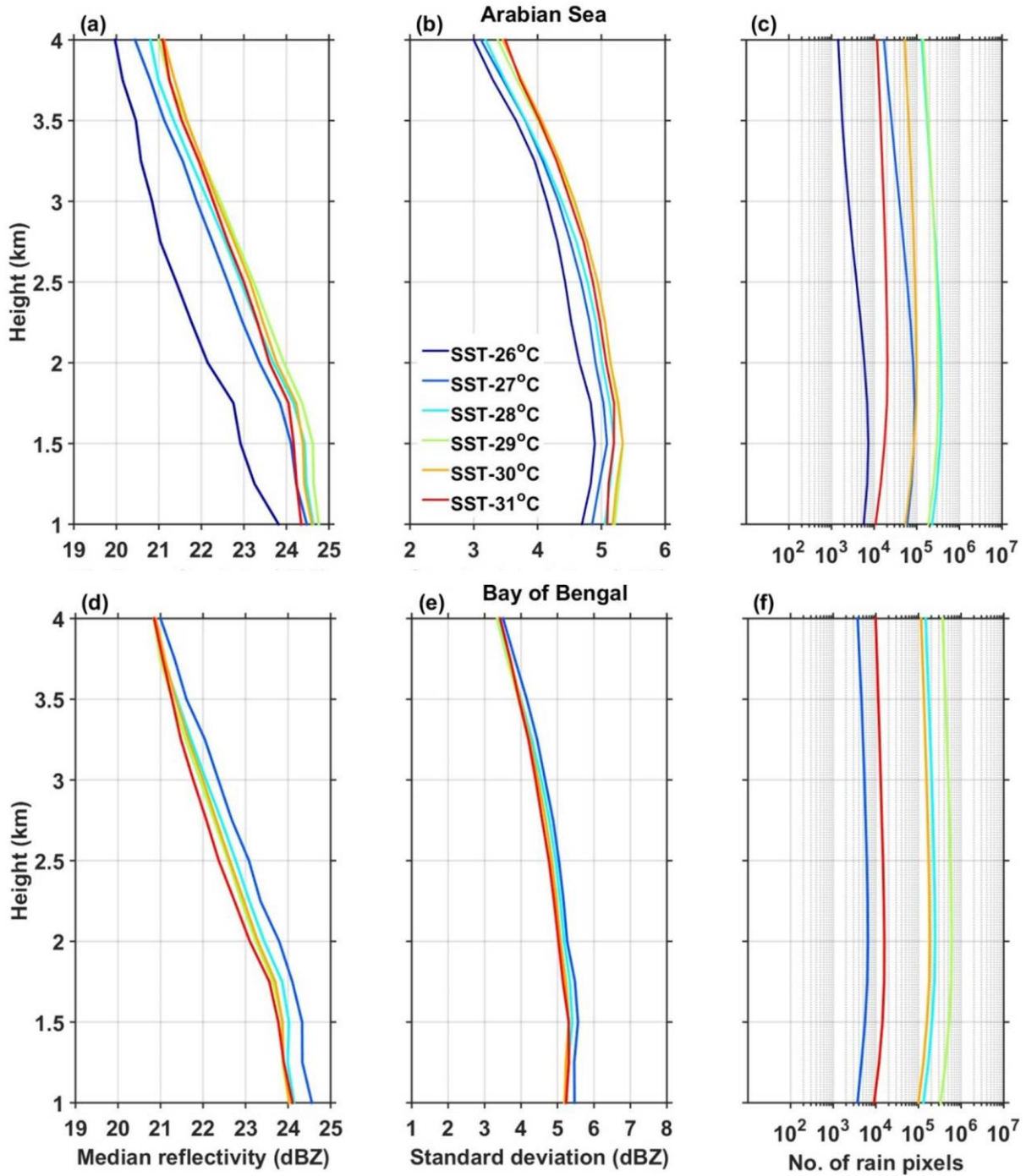
656

657 **Figure 3:** (a), (d) and (b), (e) represent vertical profiles of median reflectivity correspond to
 658 deep systems and their standard deviation (in dBZ) with SST over the AS and the
 659 BOB, respectively during the ISM season. (c) and (f) show the number of conditional
 660 reflectivity pixels at each altitude used for the estimation of the median and
 661 standard deviation.

662

663

664



665

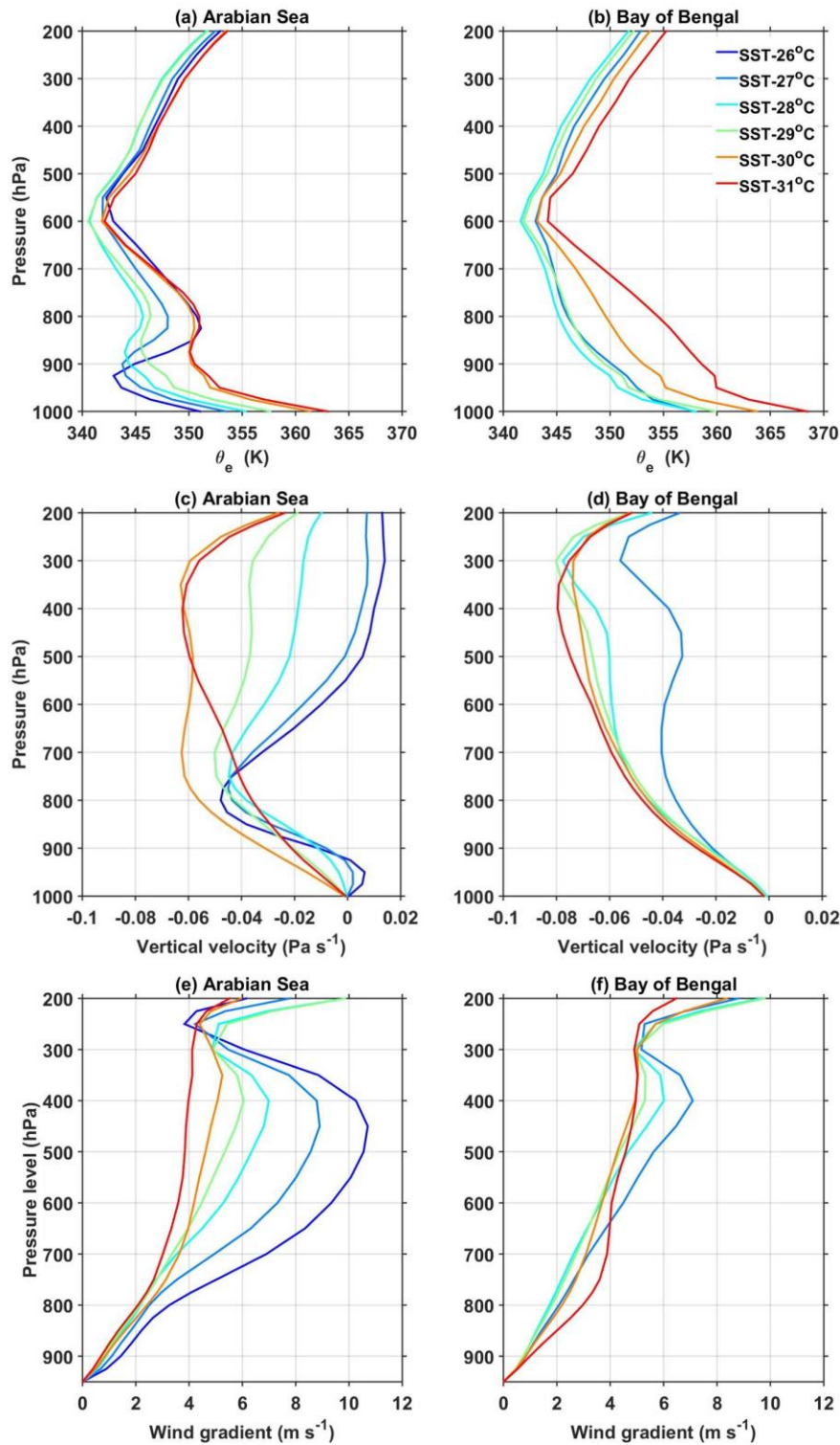
666 **Figure 4:** Same as Fig. 3 but for shallow precipitating systems.

667

668

669

670
 671
 672
 673
 674
 675
 676
 677
 678
 679
 680
 681
 682
 683
 684
 685
 686
 687
 688
 689
 690
 691
 692
 693
 694
 695
 696



697 **Figure 5:** (a) and (b), respectively, represent the vertical profiles of mean θ_e (in K) with SST
 698 over the AS and the BOB during the ISM season. (c) and (d) and (e) and (f) are same
 699 as (a) and (b) but for mean vertical velocity (in Pa s^{-1}) and wind gradient with
 700 reference to 950 hPa level (in m s^{-1}).

701
702
703
704
705
706
707
708
709
710
711
712
713
714
715
716
717
718
719
720
721
722
723
724
725
726
727
728
729
730
731

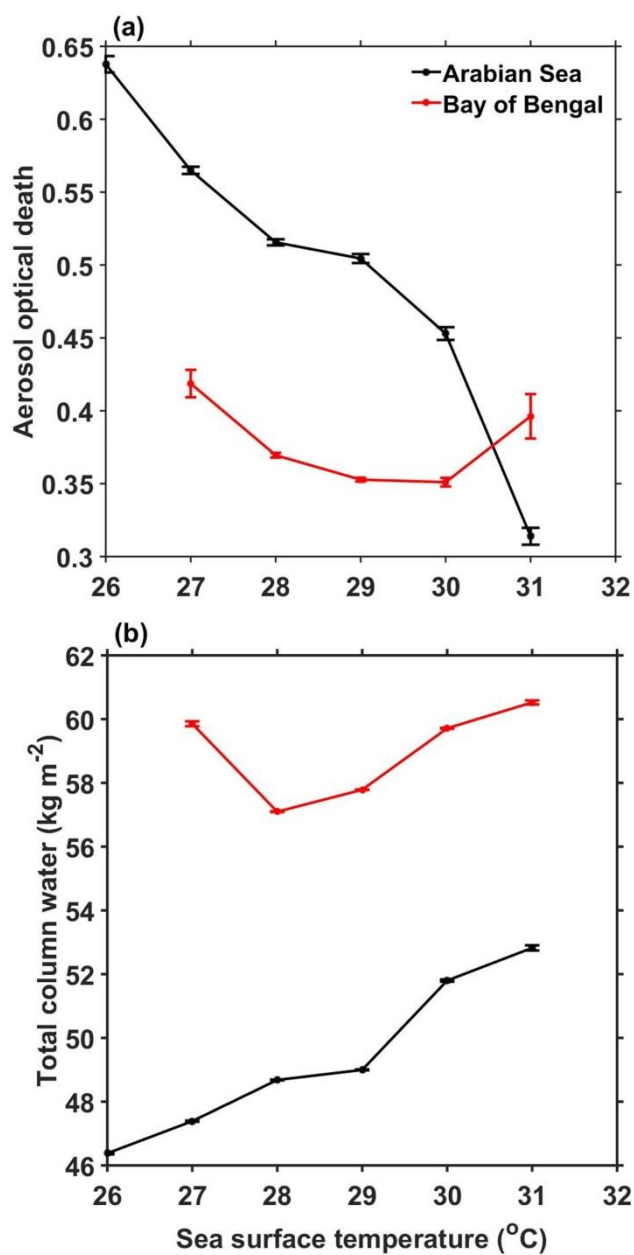


Figure 6: (a) Mean and standard error of AOD and (b) TCW (in kg m⁻²) with SST over the AS and the BOB during ISM.

732

733

734

735

736

737

738

739

740

741

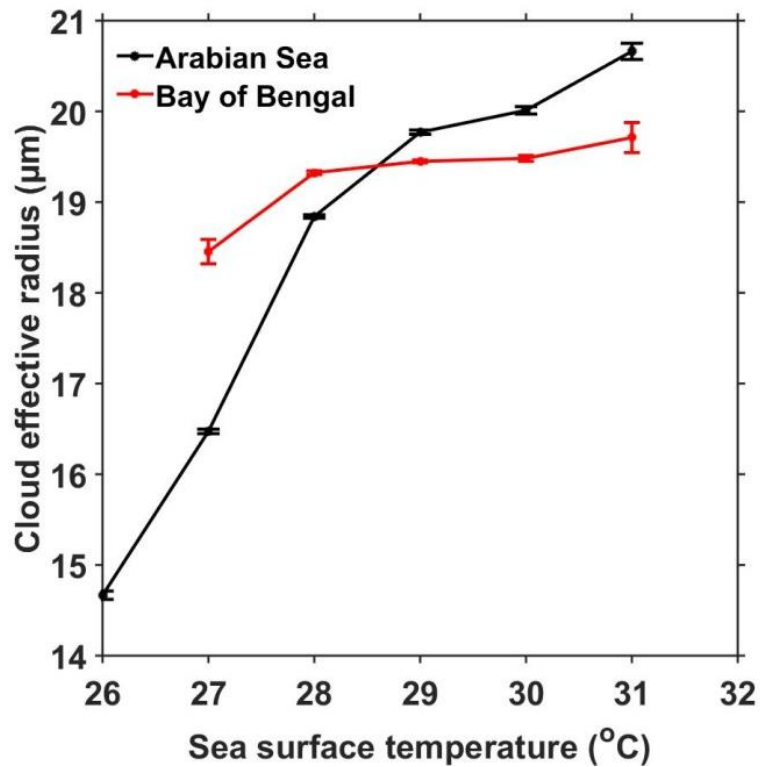
742

743

744

745

746



747 **Figure 7:** Variation of mean and standard error of CER liquid (in μm) with SST over the AS
748 and the BOB during the ISM season.

749

750